Direct observation of altermagnetic band splitting in CrSb thin films

S. Reimers,[1] L. Odenbreit,[1] L. Šmejkal,[1] V. N. Strocov,[2] C. Constantinou,[2] A. B. Hellenes,[1] R. Jaeschke Ubiergo,[1] W. H. Campos,[1] V. K. Bharadwaj,[1] A. Chakraborty,[1] T. Denneulin,[3] Wen Shi,[3] R. E. Dunin-Borkowski,[3] S. Das,[4,5] I. Mazin,[4,5] J. Sinova,[1] M. Kläui,[1] and M. Jourdan*[1]

[1] *Institut für Physik, Johannes Gutenberg-Universität Mainz, 55099 Mainz, Germany*
[2] *Paul Scherrer Institut, CH-5232 Villigen PSI, Switzerland*
[3] *Ernst Ruska-Centre for Microscopy and Spectroscopy with Electrons, Forschungszentrum Jülich, 52425Jülich, Germany*
[4] *Department of Physics and Astronomy, George Mason University, Fairfax, VA 22030*
[5] *Center for Quantum Science and Engineering, George Mason University, Fairfax, VA 22030*

Altermagnetism describes collinear ordered magnetic materials with alternating spin polarization both in real and reciprocal space. This corresponds to a distinct alternating band splitting in proximity to the Fermi energy, which we investigate directly through spin-integrated soft X-ray angular resolved photoemission spectroscopy. The experimentally obtained angle-dependent photoemission intensity, acquired from epitaxial thin films of the predicted altermagnet CrSb, demonstrates robust agreement with corresponding band structure calculations. In particular, we observe the distinctive splitting of an electronic band on a low-symmetry k-space path that connects two points featuring symmetry-induced degeneracy. The measured large magnitude of the spin splitting of approximately 0.6 eV and the position of the band just below the Fermi energy underscores the significance of altermagnets for spintronics based on spin currents.

* email: Jourdan@uni-mainz.de

INTRODUCTION

Altermagnets (AMs) represent a newly recognized subgroup of magnetically ordered materials with a collinear alignment of identical magnetic moments, which exhibit an alternating spin polarization pattern within the electronic bands in reciprocal space [1–4]. This exceptional property has sparked substantial interest in exploring innovative applications in the realm of spintronics. The goal is to harness the combined advantages presented by antiferromagnets (AFs), encompassing ultrafast dynamics [5] and resilience in the presence of external fields [6], all while capitalising on the substantial transport effects [7–10] conventionally ascribed solely to spin-polarized currents observed in ferromagnets and ferrimagnets. Consequently, these materials have the potential to lay the foundation for groundbreaking device concepts. In a manner akin to conventional collinear antiferromagnets, AMs are comprised of two sublattices that exhibit ferromagnetic ordering, featuring mutually antiparallel alignment of their magnetic moments. Nevertheless, in contrast to conventional antiferromagnets, the crystallographic sites of these two sublattices are interconnected through a combined translational and rotational symmetry operation. This operation disrupts the parity-time reversal symmetry and corresponds to a rotation of the real-space local environments of the sublattices in relation to each other. As a result, the combined crystal electric field (CEF) and exchange interactions induce an alternating spin-splitting within the electronic bands. Comparable effects have been theoretically predicted for materials exhibiting non-collinear magnetic ordering, which breaks both time and crystal symmetry, as discussed in previous works [11–14]. In conventional collinear antiferromagnets (AFMs), characterized by sublattices connected through inversion or translation with time reversal symmetry, the spin-splitting in reciprocal space is notably absent. The spin-splitting phenomenon observed in AMs holds profound relevance in the context of spintronics, as it has the potential to generate substantial spin currents. These currents have been proposed for applications such as manipulating the magnetic order within a ferromagnetic layer positioned on top of an AM layer, as outlined in Ref.[15]. In line with this, experimental confirmation of altermagnetism has been substantiated through the detection of a spin torque stemming from the anticipated AM material RuO_2 [16–18]. Additionally, as expected for AMs, the observation of an anomalous Hall effect has been documented not only in RuO_2, as discussed in Ref. [19], but also in MnTe, as reported in [20, 21]. For RuO_2, recent experimental observation of a magnetic circular dichroism in angle-resolved photoemission spectra have provided evidence for an altermagnetic band structure [22]. However, the magnitude of the altermagnetic band-splitting and the precise positioning of the relevant states with respect to the Fermi surface remain uncharted territories in experimental observations. Only for MnTe, experimental evidence for altermagnetic band splitting, though well below the Fermi energy, was recently reported [23–25]. In the context of AMs for spintronics, the primary goal is to attain a substantial spin-splitting within the conduction bands in close proximity to the Fermi surface. While in conventional antiferromagnets spin-

splitting originates from spin-orbit coupling with maximum observed values of $\simeq$ 100 meV [27], for AMs, density functional theory (DFT) calculations have prediced a one order of magnitude larger the spin splitting of the valence bands. Given the paramount importance of this parameter in the realm of spintronic applications, the validation of this spin-splitting magnitude through experimental means becomes indispensable in comprehensively evaluating the potential of altermagnets for spintronics. In this study, we delve into an exploration of the electronic bands in epitaxial thin films of the altermagnet CrSb. We employ spin-integrated soft X-ray angular-resolved photoelectron spectroscopy (SX-ARPES) to probe these bands and compare our findings with band structure calculations.

RESULTS AND DISCUSSION

Altermagnetic band splitting in CrSb

Among metallic altermagnets, CrSb distinguishes itself by large predicted band splitting [4] and an ordering temperature significantly exceeding room temperature. Hexagonal CrSb orders magnetically at T_N=700 K [26] with ferromagnetic (001) planes, which are coupled antiferromagnetically along the easy c-axis [29]. Figure 1, panel **a**, depicts the crystal structure of the compound. Panel **b** zooms into the local crystallographic environment of the magnetic sublattices. Along the c-axis, the triangular arrangements of the Sb atoms above and below each Cr sublattice are rotated by 60° with respect to each other. This is the origin of the for each Cr sublattice different orientation of the anisotropic crystal electric field (CEF), which is essential for altermagnetism.

Panel **c** shows the Brillouin zone (BZ) of CrSb, in which three k-space paths discussed below are indicated. Previous calculations have predicted significant altermagnetic band splitting, along the low-symmetry path Γ-L [3]. Here, we consider in particular the likewise low symmetry Q-P path, as this direction is best accessible with our experimental geometry.

The corresponding band structure, calculated without spin-orbit coupling (SOC), shows a large altermagnetic band splitting (Fig 1**d**). SOC induces minor additional band shifts only (panel **e**), thus, it is not significant for the formation of the altermagnetic band splitting indicated by the pink arrows. To demonstrate the role of the exchange interaction for the formation of the altermagnetic BS, we show in panel **f** a non-magnetic calculation of CrSb. Again, the anisotropic CEF results in a energy splitting of the projections of the electronic states on the crystallographically distinct Cr sublattices. However, compared to the altermagnetic case, the bands show a qualitatively very different dispersion. Thus, the exchange interaction does not just add rigid spin dependent energy shifts to the bands, i. e. , it is **k**-dependent.

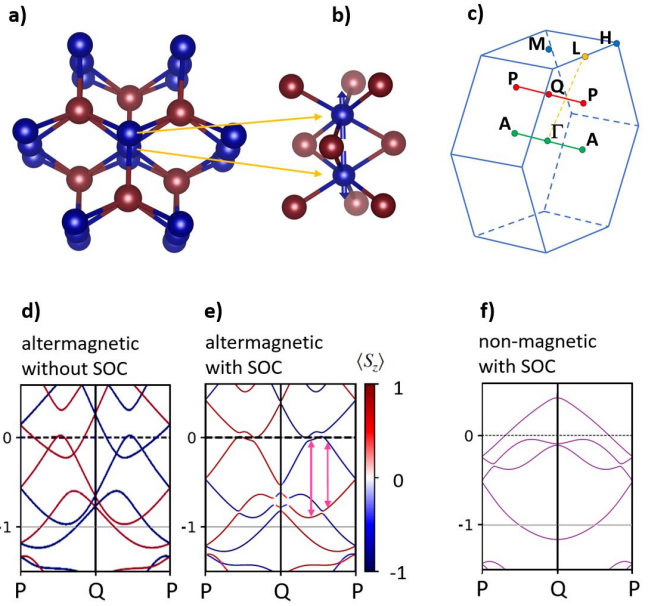

FIG. 1. **Structure of CrSb. a)** Crystal structure. Blue: Cr atoms, Red: Sb atoms. Drawn with VESTA [28]. **b)** Local environment of the Cr sublattices with antiparallel alignment of the magnetic moments. **c)** Brillouin zone of CrSb showing, e. g., the P-Q-P path, for which altermagnetically split bands are expected. **d)** Altermagnetic band structure calculations without SOC for the P-Q-P path. The color of the bands indicates the spin polarization. **e)** Altermagnetic band structure calculations with SOC for the P-Q-P path. **f)** Band structure of the non-magnetic state (with SOC).

The electronic states within high-symmetry planes, encompassing the Q and P points, display degeneracy. Consequently, along the high-symmetry k-space paths conventionally investigated by ARPES, the altermagnetic band splitting is absent. Along these directions, our calculations align closely with previously reported findings [30]. Nonetheless, for the low-symmetry path that links Q and P, as previously discussed (Fig. 1, **d** and **e**), substantial spin splitting of the bands is anticipated. To confirm the validity of the band structure calculations, and in particular to probe the magnitude of the altermagnetic band splitting, we perform SX-ARPES investigations of epitaxial CrSb(100) thin films.

Band structure investigation by SX-ARPES

The analysis of ARPES data hinges on the accurate identification of distinctive directions in reciprocal space. Thus, it becomes imperative to experimentally ascertain the characteristic high-symmetry points within the Brillouin zone. We identify the centre of the Brillouin zone (Γ-point) by scanning the photon energy, which corresponds to a scan in k-space along the direction perpendicular to the CrSb(100) sample surface. The resulting ARPES intensity $I(\mathbf{k})$ at the Fermi energy is shown in Fig. 2, panel **a**, and correspond to a cut through the Fermi

surface in the Γ-M-K plane. A cut through the perpendicular Γ-K-A plane, measured with a fixed photon energy (775 eV) selecting one of the Γ-points from panel **a**, is shown in panel **b**. Both 2-dimensional constant-energy $I(\mathbf{k})$ cuts at the Fermi energy are in good agreement with the calculated 3-dimensional Fermi surface shown in panel **c**, providing evidence for the validity of the calculation and quality of the samples. The observed strong variation of the ARPES intensity from different Brillouin zones will be discussed below.

We now discuss specific directions in k-space with and without altermagnetic band splitting and contrast the ARPES intensity $I(E, \mathbf{k})$ with band structure calculations for selected paths traversing the Brillouin zone. To enhance the comparability with the experimental data, we incorporate spin-orbit coupling (SOC) into the calculations. While the angle-dependent photoemission intensity does not precisely replicate the electronic band structure owing to distinct photoemission matrix elements [31], it does allow for the direct observation of distinctive band structure features. To investigate the altermagnetic band splitting in the CrSb(100) films using ARPES, we specifically opt for the Q-P path, as shown in Fig. 1. This chosen path is aligned parallel to the sample surface, facilitating the direct imaging of the corresponding ARPES intensity $I(E, \mathbf{k})$ with our experimental detector setup. This low-symmetry path with large altermagnetic spin-splitting is parallel to the high symmetry Γ-A path, which shows no CEF driven spin splitting. Consequently, we can measure both paths in k-space with the same experimental geometry but different photon energies, selecting different values of k_z. Since the wave vector $\mathbf{k}$ of the photoemitted electrons resides within a crystallographic mirror plane of CrSb (as illustrated in Supplementary, Fig. S3), we take into consideration the parity selection rules [32] by acquiring spectra with both p- and s-polarized photons. Furthermore, the ARPES data contains an ±k asymmetry induced by the 20° grazing photon incidence from the positive k-value side in Figs. 3 and 4 (see Supplementary, Fig. S3, panel **a**).

Figure 3 presents a comparison between the ARPES intensity $I(E, \mathbf{k})$ and band structure calculations for both k-space paths discussed above. The background subtracted ARPES raw data covering three Brillouin zones is shown together with the superimposed band structure calculations in the same plot. To provide a comprehensive understanding of the relationship between ARPES intensity and band structure calculations for CrSb, we first discuss the overall data trends acquired over a wider energy range.

For the high-symmetry Γ-A path (panels **a** and **b**), the consistency between the ARPES data and the band structure calculations is evident, irrespective of the chosen Brillouin zone and photon polarization. In all figures, the calculated band structure's energy scale has been rigidly shifted by approximately 150 meV to enhance alignment. Additional shifts of specific bands may be attributed to electronic correlation effects not accounted for in the calculation.

For the low-symmetry Q-P path (panels **c** and **d**), the situation is more complex. Here, a pronounced polarization dependence and a forward-backward scattering asymmetry inherent to the ARPES geometry (see Methods) is discernible. Furthermore, for this path, a strong alternation of the ARPES intensity from Brillouin zones to Brillouin zone is observed. These effects are embedded in the matrix elements describing the transition from the occupied to the photoemitted electronic states [31]. Nevertheless, it is possible to provide an intuitive explanation: The alternating ARPES intensity likely arises from an interference effect associated with the periodic arrangement of the Cr atoms within the CrSb unit cell (as depicted in Fig. 1**a**). These atoms alone correspond to a Brillouin zone that is doubled along the c-direction compared to the actual full CrSb cell. The inclusion of the Sb atoms can be viewed as a minor perturbation, which primarily preserves the physical scattering potential of the Cr-only states. However, formally, it leads to the folding of the Cr bands into a Brillouin zone half the size of the original CrSb Brillouin zone. In ARPES, this translates into a periodicity of the photoemission intensity that aligns with the doubled formal Brillouin zone. Thus, bands with a strongly alternating ARPES intensity have mainly Cr character. However, when taking into account both photon polarizations and all Brillouin zones collectively, the experimental data is consistent with the band structure calculations across a broad spectrum of binding energies for the Q-P path.

Altermagnetic band splitting observed by SX-ARPES

Now, we narrow our attention to the energy range in proximity to the Fermi energy, a region where the altermagnetic band splitting is anticipated and holds particular relevance for practical applications. Within our experimental setup, direct observation of the altermagnetic band splitting becomes feasible for the Q-P path, as depicted in Fig. 4. The most significant splitting is highlighted by the pink arrows in the superimposed band structure calculation. Within the ARPES data, the majority of bands are most distinctly observable within the central Brillouin zone, particularly when employing p-polarized photons, as shown in panel **a** and backward scattering (photon grazing incidence from positive k-value direction). In this context, the energetically lower branch of altermagnetically split band is prominently discernible in the experimental data. Conversely, when employing s-polarized photons, as displayed in panel **b**, this lower branch is notably absent, indicating the presence of an essentially even-parity state with respect to

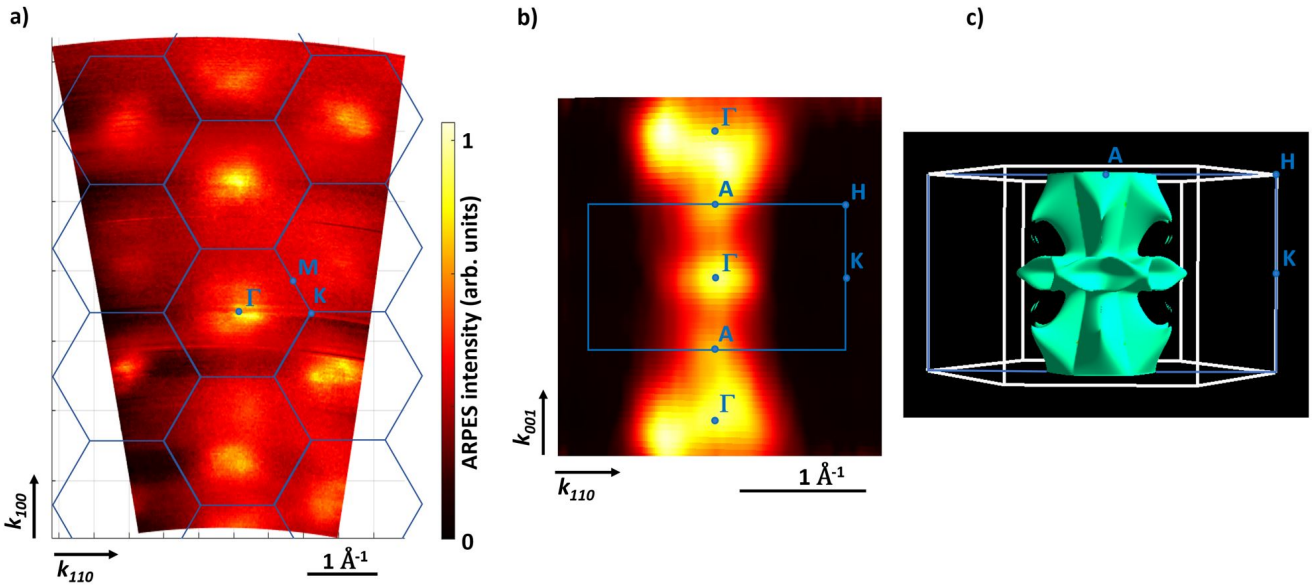

FIG. 2. **Experimental and theoretical Fermi surface of CrSb.** Comparison of the SX-ARPES intensity $I(\mathbf{k})$ at the Fermi energy obtained in the Γ-M-K plane (panel **a**) and in the Γ-K-A plane (panel **b**) with the calculated 3-dimensional Fermi surface shown in panel **c**. The corresponding Brillouin zone and high symmetry points are superimposed for clarity.

the scattering plane as discussed in detail in the Supplementary material. The anticipated energetically higher branch of the split band is less conspicuous in the experimental data and becomes overshadowed by the forward-backward scattering asymmetry. Therefore, in panels **c** and **d**, we present the ARPES results from the central Brillouin zone acquired with p-polarized photons after symmetrization and filtering. With this procedure, both branches of the altermagnetically split band become discernible in the raw data. To enhance visibility and pinpoint the centers of the split band branches with greater precision, we have computed a Laplacian image the ARPES raw data. The application of the Laplace operator enhances the positions of maximum curvature within the ARPES intensity (see Methods). Consequently, the distinctive features of both branches become pronounced, allowing for a comprehensive comparison with the band structure calculations superimposed onto the experimental data:

In panel **c**, the measured ARPES intensity is partially superimposed with the altermagnetic BS calculation for comparison. Good agreement of the main features is obtained. In particular, the altermagnetic band splitting, as indicated by the pink arrows in the calculation, is now conspicuously evident in the experimental data. The lower branch of this splitting, which was already discernible in the non-symmetrized ARPES raw data (central Q-P path in Fig. 4**a**) aligns remarkably well with a region of elevated ARPES intensity. Conversely, the upper branch appears faint in the raw data, but becomes now distinctly discernible. It is positioned approximately 200 meV lower in energy compared to the band structure calculated, presumably due to the effect of electronic correlations not covered in the calculation.

For comparison, we show in panel **d** the superposition of the non-magnetic BS calculation (see also Fig. 1**f**) with the experimental ARPES data, disclosing a lack of consistency. This is most obvious in the region of highest ARPES intensity around the Q point at a binding energy of $\simeq 1$ eV and in the region where the upper branch of the altermagnetically split band has been identified in panel **c**.

In summary, we obtained good agreement of the experimental SX-ARPES intensity with calculations revealing an altermagnetic band structure of CrSb. In particular, we have detected band degeneracy at specific k-space points situated on high-symmetry planes perpendicular to the c-axis. These planes encompass Q within the central plane containing the Γ point and P, which is positioned at the boundary of the Brillouin zone. Along the trajectory that connects these points, we observe the anticipated altermagnetic band splitting.

The fundamental hallmark of altermagnetism lies in such spin splitting of electronic valence bands, for which our results furnish direct experimental evidence focusing on CrSb. Interestingly, similar results were reported very recently for MnTe [24]. However, CrSb stands out due to the significant magnitude of the band splitting, quantified at 0.6 eV in our measurements, and the notable energetic placement of the strongly split band positioned just below the Fermi energy. This specific energetic positioning holds crucial significance in the context of potential

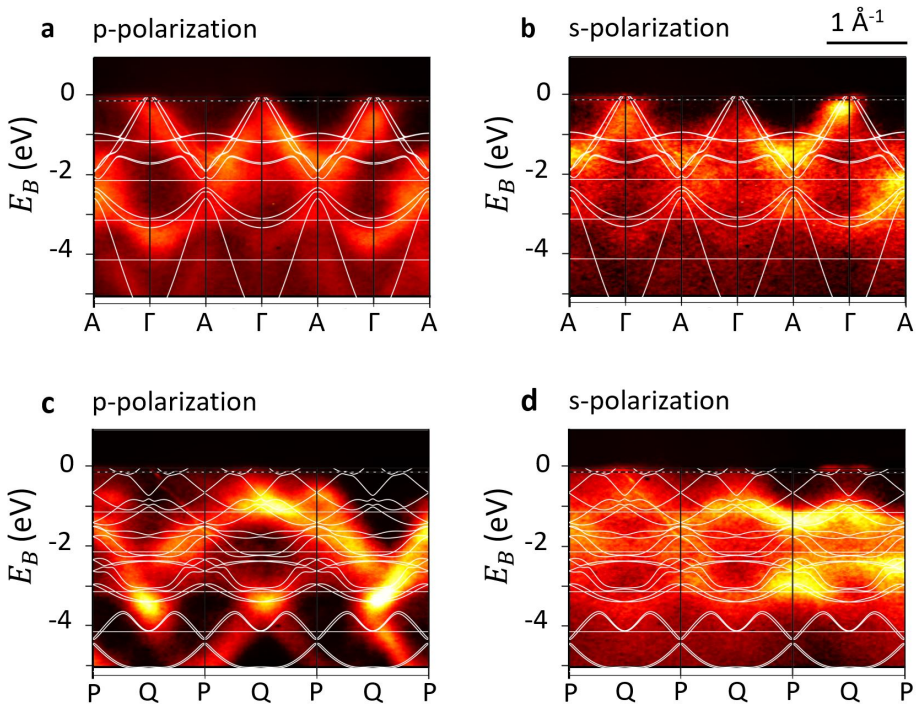

FIG. 3. **Wide energy range ARPES intensity and band structure calculations.** The SX-ARPES intensity $I(E, \mathbf{k})$ is shown with the corresponding superimposed band structure calculations. **a**: High symmetry Γ-A path with p-polarized photons. **b**: Γ-A path with s-polarized photons. **c**: Low symmetry Q-P path with p-polarized photons. **b**: Q-P path with s-polarized photons.

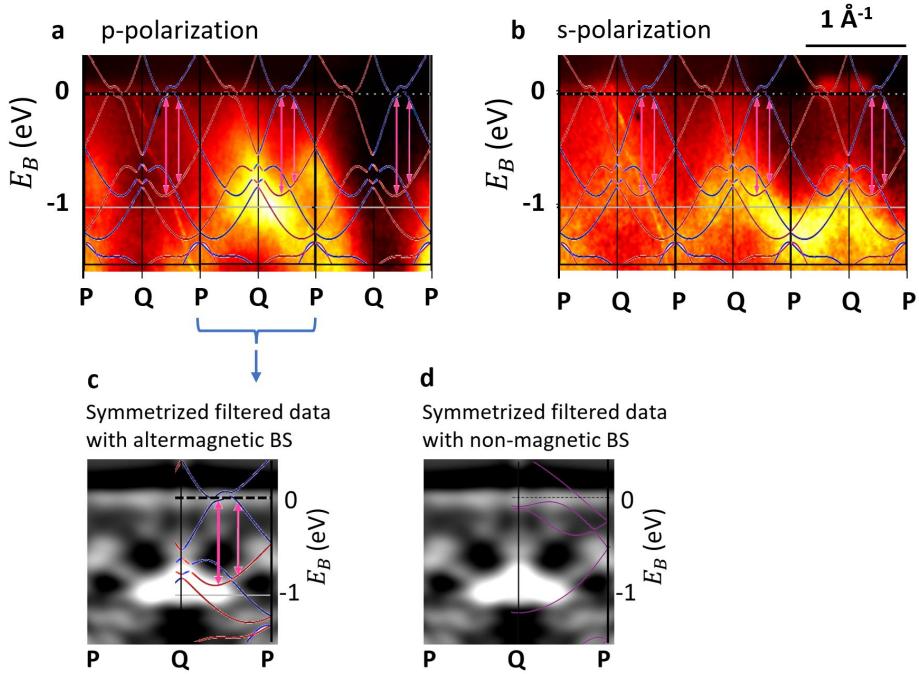

FIG. 4. **Band splitting near the Fermi energy.** The spin integrated SX-ARPES intensity $I(E, \mathbf{k})$ just below the Fermi energy is shown with the corresponding superimposed spin resolved band structure calculations. **a**: High symmetry P-Q path with p-polarized photons. **b**: P-Q path with s-polarized photons. Panel **c** shows the symmetrized ARPES intensity (after application of an Laplacian filter enhancing the visibility of the bands) from the central Brillouin zone for p-polarization with the superimposed altermagnetic BS calculation. Panel **d** show the same data superimposed with the non-magnetic BS calculation.

spin-polarized currents. Consequently, our results establish the fundamental groundwork for potential spintronic applications leveraging the emerging class of altermagnetic materials.

METHODS

Film preparation

Epitaxial CrSb(100) thin films of 30 nm thickness were grown by dc magnetron sputtering from a single multi-segment Cr/Sb target on GaAs(110) substrates. After deposition at a substrate temperature of $\simeq 300^{o}$C, the sample was annealed in-situ at a temperature of $\simeq 400^{o}$C for 15 min. As shown in the Supplementary Material by X-ray and electron diffraction as well as by transmission electron microscopy, the thin films are fully epitaxial with the in-plane hexagonal c-axis of CrSb(100) aligned parallel to the in-plane (001)-direction of the GaAs(110) substrate.

SX-ARPES measurements and data evaluation

After the electron diffraction (reflection high-energy electron diffraction, RHEED) based confirmation of a structurally well-ordered sample surface (Supplementary Material), the epitaxial thin films were transported to the ARPES endstation using a vacuum suitcase. The SX-ARPES investigations were performed at the ADRESS beamline [33, 34] of the Swiss Light Source. The ARPES endstation uses an experimental geometry with 20^{o} grazing light incidence angle. As the direction of light incidence and the angle dispersive direction (detector slit orientation) are in the same plane, this creates a forward-backward scattering asymmetry in the photoemission intensity. The measurements were conducted at a temperature of 12 K, with varying the photon energy from 320 eV to 1000 eV. Γ points were identified, e. g., at photon energies of 775 eV and 935 eV. The total energy resolution including thermal broadening amounts to approx. 100 meV in this energy range. All ARPES data shown in this manuscript was visualized using the Matlab program ARPESView (by V. Strocov, [35]), which subtracts an angle-integrated background from the raw data. Beyond this, panel **c** of Fig. 4 shows symmetrized data, i. e., the ARPES image was mirrored along the $k_z = 0$ axis and added to the original data. The band enhancement shown in the right figure of panel **c** was obtained using the Fiji distribution of the image processing software ImageJ, specifically by applying the function FeatureJ: Laplacian.

Band structure calculations

The experimental results were compared with calculations based on ab initio spin-density functional theory with local-density approximation. The spectral function of CrSb(001) was computed for an infinite system using the fully relativistic Korringa-Kohn-Rostoker method as implemented in the Munich SPR-KKR package [36, 37].

Data availability

The raw data of the transport measurements generated in this study have been deposited in the Zenodo database under accession code ???.

Acknowledgements

We acknowledge support by H.-J. Elmers (JGU Mainz) for the Laplacian filter application.

We acknowledge funding by the Deutsche Forschungsgemeinschaft (DFG, German Research Foundation) - TRR 173 - 268565370 (project A05 (M.J.), with contribution from A01 (M.K.)), by the Horizon 2020 Framework Program of the European Commission under FET-Open Grant No. 863155 (s-Nebula) (M.K.), by EU HORIZON-CL4-2021-DIGITAL-EMERGING-01-14 programme under grant agreement No. 101070287 (M.K.), and by the TopDyn Center (M.K.). We acknowledge the Swiss Light Source for time on beamline ADRESS under Proposal 20222058 (M.J.). The STEM investigations were funded by the European Union's Horizon 2020 Research and Innovation Programme under grant agreement 856538 (project "3D MAGIC") (M.K. and R.E.D.-B.).

Author contributions

S.R. and M.J. wrote the paper. S.R., L.O. and M.J. prepared the samples and performed and evaluated the SX-ARPES investigations supported by V.N.S. and C.C.. L.S., A.B.H., R.J.U., W.H.H., V.K.B., and A.C. provided the band structure calculations. S.D. and I.M. provided the Fermi surface calculation. T.D., W.S. and R.E.D-B contributed the STEM investigations. J.S. and M.K. contributed to the discussion of the results and provided input, M.J. coordinated the project.

Competing interests:

The authors declare no competing financial interests.

[1] Šmejkal, L., González-Hernández, R., Jungwirth, T., and Sinova, J. Crystal time-reversal symmetry breaking and spontaneous Hall effect in collinear antiferromagnets. *Sci. Adv.* **6**, eaaz8809 (2020).

[2] Hayami, S., Yanagi, Y., Kusunose, H. Momentum-Dependent Spin Splitting by Collinear Antiferromagnetic Ordering. *J. Phys. Soc. Jpn.* **88**, 123702 (2019).

[3] Šmejkal, L., Sinova, J., Jungwirth, T Beyond Conventional Ferromagnetism and Antiferromagnetism: A Phase with Nonrelativistic Spin and Crystal Rotation Symmetry, *Phys. Rev. X* **12**, 031042 (2022).

[4] Šmejkal, L., Sinova, J., Jungwirth, T. Emerging Research Landscape of Altermagnetism, *Phys. Rev. X* **12**, 040501 (2022).

[5] Kampfrath, T., Sell, A., Klatt, G., Pashkin, A., Mährlein, S., Dekorsy, T., Wolf, M., Fiebig, M., Leitenstorfer, A., and Huber, R. Coherent terahertz control of antiferromagnetic spin waves, *Nat. Phot.* **5**, 31 (2011).

[6] Bodnar, S. Yu., Skourski, Y., Gomonay, O., Sinova, J., Kläui, M., Jourdan, M. Magnetoresistance Effects in the Metallic Antiferromagnet Mn_2Au. *Phys. Rev. Appl.* **14**, 014004 (2020).

[7] Shao, D.-F., Zhang, S. H., Li, M., Eom, C. B., Tsymbal, E. Y. Spin-neutral currents for spintronics, *Nat. Commun.* **12**, 7061 (2021).

[8] Gurung, G., Shao, D.-F., Tsymbal, E. Y. Transport spin-polarization of noncollinear antiferromagnetic antiperovskites. *Phys. Rev. Mat.* **5** 124411 (2021).

[9] Šmejkal, L., Hellenes, A. B., González-Hernández, R., Sinova, J., Jungwirth, T. Giant and Tunneling Magnetoresistance in Unconventional Collinear Antiferromagnets with Nonrelativistic Spin-Momentum Coupling, *Phys. Rev. X* **12**, 011028(2022).

[10] Gurung, G., Shao, D.-F., Tsymbal, E. Y. Extraordinary Tunneling Magnetoresistance in Antiferromagnetic Tunnel Junctions with Antiperovskite Electrodes, arXiv:2306.03026 (2023).

[11] Železný, J., Zhang, Y., Felser, C., Yan, B., Spin-Polarized Current in Noncollinear Antiferromagnets *Phys. Rev. Lett.* **119** 187204 (2017).

[12] Suzuki, M.-T., Koretsune, T., Ochi, M., Arita, R. Cluster multipole theory for anomalous Hall effect in antiferromagnets. *Phys. Rev. B* **95** 094406 (2017).

[13] Yuan, L.-Z., Wang, Z., Luo, J.-W., Rashba, E. I., Zunger, A. Giant momentum-dependent spin splitting in centrosymmetric low-Z antiferromagnets. *Phys. Rev. B* **102** 014422 (2020).

[14] Chen, H., Niu, Q., MacDonald, A. H. Anomalous Hall Effect Arising from Noncollinear Antiferromagnetism. *Phys. Rev. Lett.* **112** 017205 (2014).

[15] González-Hernández, R., Šmejkal, L., Výborný, K., Yahagi, Y., Sinova, J., Jungwirth, T., and Železný, J. *Phys. Rev. Lett.* **126** (2021).

[16] Bose, A., Schreiber, N. S., Jain, R. J.,Shao, D. F., Nair, H. P., Sun, J., Zhang, X. S., Muller, D. A., Tsymbal, E. Y., Schlom, D. G., Ralph, D. C. Tilted spin current generated by the collinear antiferromagnet ruthenium dioxide. *Nat. Electr.* **267** (2022).

[17] Bai, H., Feng, X. Y., Zhou, Y. J., Su, R. X., Liao, L. Y., Zhu, W. X., Chen, X. Z., Pan, F., Song, C. Observation of Spin Splitting Torque in a Collinear Antiferromagnet RuO_2. *Phys. Rev. Lett.*, **128**, 197202 (2022).

[18] Karube, S., Tanaka, T., Sugawara, D., Kadoguchi, N., Kohda, M., Nitta, J. Observation of Spin-Splitter Torque in Collinear Antiferromagnetic RuO_2. *Phys. Rev. Lett* **129**, 137201 (2022).

[19] Feng, Z., Zhou, X., Šmejkal, L., Wu, L., Zhu, Z., Guo, H., González-Hernández, R., Wang, X., Yan, H., Qin, P., Zhang, X. Wu, H., Chen, H., Meng, Z., Liu, L., Xia, Z., Sinova, J., Jungwirth, T., Liu, Z. An anomalous Hall effect in altermagnetic ruthenium dioxide. *Nat. Electr.* **5**, 735 (2022).

[20] Reichlová, H., Seeger, R. L., González-Hernández, R., Kounta, I., Schlitz, R., Kriegner, D., Ritzinger, P., Lammel, M., Leiviskä, M., Petříček, V., Doležal, P., Schmoranzerová, E., Bad'ura, A., Thomas, A., Baltz, V., Michez, L., Sinova, J., Goennenwein, S., Jungwirth, T., Šmejkal, L. Macroscopic time reversal symmetry breaking arising from antiferromagnetic Zeeman effect. arXiv:2012.15651 (2021).

[21] González-Betancourt, R. D., Zubáč, J., González-Hernández, R., Geishendorf, K., Šobáň, Z., Springholz, G., Olejník, K., Šmejkal, L., Sinova, J., Jungwirth, T., Goennenwein, S. T. B., Thomas, A., Reichlová, H., Železný, J., Kriegner, D. Spontaneous Anomalous Hall Effect Arising from an Unconventional Compensated Magnetic Phase in a Semiconductor. *Phys. Rev. Lett.* **130**, 036702 (2023).

[22] Fedchenko, O., Minár, J., Akashdeep, A., D'Souza, S. W., Vasilyev, D., Tkach, O., Odenbreit, L., Nguyen, Q. L., Kutnyakhov, D., Wind, N., Wenthaus, L., Scholz, M., Rossnagel, K., Hoesch, M., Aeschlimann, M., Stadtmüller, B., Kläui, M., Schönhense, G, Jakob, G., Jungwirth, T., Šmejkal, L., Sinova, J., Elmers, H. J. Observation of time-reversal symmetry breaking in the band structure of altermagnetic RuO_2. arXiv:2306.02170 (2023).

[23] Osumi, T., Souma, S., Aoyama, T., Yamauchi, K., Honma, A., Nakayama, K., Takahashi, T., Ohgushi, K., Sato, T. Observation of Giant Band Splitting in Altermagnetic MnTe. arXiv:2308.10117v1 (2023).

[24] Krempaský, J., Šmejkal, L., D'Souza, S. W., Hajlaoui, M., Springholz, G., Uhlírová, K., Alarab, F., Constantinou, P. C., Strokov, V., Usanov, D., Pudelko, W. R., González-Hernández, R., Birk Hellenes, A., Jansa, Z., Reichlová, H., Šobášvn, Z., Gonzalez Betancourt, R. D., Wadley, P., Sinova, J., Kriegner, D., Minár, J., Dil, J. H. and Jungwirth, T. Altermagnetic lifting of Kramers spin degeneracy. arXiv:2308.10681v1 (2023).

[25] Lee, Suyoung, Lee, Sangjae, Jung, Saegyeol, Jung, Jiwon, Kim, Donghan, Lee, Yeonjae, Seok, Byeongjun, Kim, Jaeyoung, Park, Byeong Gyu, Smejkal, Libor, Kang, Chang-Jong, and Kim Changyoung, Broken Kramers' Degeneracy in Altermagnetic MnTe. arXiv:2308.11180v1 (2023).

[26] Takei, W. J., Cox, D. E., and Shirane, G. Magnetic Structures in the MnSb-CrSb System. *Phys. Rev.* **129**, 2008 (1963).

[27] Elmers, H. J., Chernov, S. V., D'Souza, S. W., Bommanaboyena, S. P., Bodnar, S. Yu., Medjanik, K., Babenkov, S., Fedchenko, O., Vasilyev, D., Agustsson, S. Y., Schlueter, C., Gloskovskii, A., Matveyev, Yu., Strocov, V. N., Skourski, Y., Šmejkal, L., Sinova, J., Minár, J., Kläui, M., Schönhense, G., and Jourdan, M. Nél Vector Induced Manipulation of Valence States in the Collinear Antiferromagnet Mn_2Au. *ACS Nano* **20**, 17554 (2020).

[28] Momma, K. and Izumi, F. VESTA 3 for three-dimensional visualization of crystal, volumetric and morphology data. *J. Appl. Crystallogr.* **44**, 1272 (2011).

[29] Snow, A. I. Neutron Diffraction Invesitgation of the Atomic Moment Orientation in the Antiferromagnetic Compound CrSb. *Phys. Rev.* **85**, 365 (1952).

[30] Park, I. J., Kwon, S., and Lake, R. K. Effects of filling, strain, and electric field on the Néel vector in antiferromagnetic CrSb. *Phys. Rev. B* **102**, 224426 (2020).

[31] Moser, S. An experimentalist's guide to the matrix element in angle resolved photoemission. *J. Electr. Spec. Rel. Phen.* **214**, 29 (2017)).

[32] Gobeli, G., Allen, F. G., and Kane, E. O. Polarization evidence for momentum conservation in photoelectricemission from germanium and silicon. *Phys. Rev. Lett.* **12**,

94 (1963).
[33] Strocov, V. N.; Schmitt, T.; Flechsig, U.; Schmidt, T.; Imhof, A.; Chen, Q.; Raabe, J.; Betemps, R.; Zimoch, D.; Krempasky, J.; Wang, X.; Grioni, M.; Piazzalunga, A.; Patthey, L. High-Resolution Soft X-Ray Beamline ADRESS at the Swiss Light Source for Resonant Inelastic X-Ray Scattering and Angle-Resolved Photoelectron Spectroscopies. *J. Synchrotron Radiat.* **17**, 631 (2010).
[34] Strocov, V. N.; Wang, X.; Shi, M.; Kobayashi, M.; Krempasky, J.; Hess, C.; Schmitt, T.; Patthey, L. Soft-X-Ray ARPES Facility at the ADRESS Beamline of the SLS: Concepts, Technical Realisation and Scientific Applications. *J. Synchrotron Radiat.* **21**, 32 (2014).
[35] https://www.psi.ch/en/sls/adress/manuals
[36] Ebert, H. Munich SPR-KKR package. www.ebert.cup.uni-muenchen.de/kkr/kkrlicense.
[37] Ebert, H., Koedderitzsch, D., Minár, J. Calculating Condensed Matter Properties Using the KKR-Greens Function Method-Recent Developments and Applications. *Rep. Prog. Phys.* **74**, 096501 (2011).